 CMES, vol.118, no.3, pp.561-581, 2019

A Non-Ordinary State-Based Peridynamic Formulation for Failure of Concrete Subjected to Impacting Loads

Liwei Wu[1], Dan Huang[1, *], Yepeng Xu[1] and Lei Wang[1]

Abstract: Strain hardening and strain rate play an important role in dynamic deformation and failure problems such as high-velocity impact cases. In this paper, a non-ordinary state-based peridynamic model for failure and damage of concrete materials subjected to impacting condition is proposed, taking the advantages of both damage model and non-local peridynamic method. The Holmquist-Johnson-Cook (HJC) model describing the mechanical character and damage of concrete materials under large strain, high strain rate and high hydrostatic pressure was reformulated in the framework of non-ordinary state-based peridynamic theory, and the corresponding numerical approach was developed. The proposed model and numerical approach were validated through simulating typical impacting examples and comparing the results with available experimental observations and results in literature.

Keywords: Non-ordinary state-based peridynamics, Holmquist-Johnson-Cook model, dynamic fracture, concrete, non-local.

1 Introduction

Concrete is a kind of widely used material in protective engineering and infrastructures, which attracts interest of researchers from nuclear industry and fortification installations [Corbett, Reid and Johnson (1996); Børvik, Langseth, Hopperstad et al. (2002)]. Since the progressive failure of internal defects will lead to the weakness of concrete structures and probably will bring a sudden destruction without visible damage, it has become a long-standing and rough challenge for researchers to study the mechanism of damage evolution, crack nucleation and propagation in concrete materials and structures. In order to ensure the structural safety, especially under impact and fatigue loadings, one should accurately describe the destruction mechanism of concrete materials and structures.

Many researches on the mechanical behavior of concrete under dynamic condition have been conducted and some simplified analytical models are determined by experiments [Kennedy (1976); Ben-Dor, Dubinsky and Elperin (2005); Li, Reid, Wen et al. (2005)]. On the other hand, numerical simulations with different constitutive models of concrete were used in penetration and impact problems [Teng, Chu, Chang et al. (2005); Leppänen (2006); Tai and Tang (2006)]. In addition, different constitutive models for concrete under dynamic loadings were investigated in Bićanić et al. [Bićanić and Zienkiewicz

[1] College of Mechanics and Materials, Hohai University, Nanjing, 211100, China.
[*] Corresponding Author: Dan Huang. Email: danhuang@hhu.edu.cn.

(2010); Liu and Ning (2008)]. However, the development of reliable and robust models describing the failure of concrete, especially in impacting cases, is still challenging.

Various efforts have been made to study the failure in concrete, but the failure mechanism of concrete materials and structures has not been fully understood yet. To describe and simulate the discontinuous problem under the framework of classical continuous mechanics theory, the difficulty derives from the mathematical formulation consisting of partial differential equations. These equations cannot be applied directly across the discontinuities resulting from the material failure, since the partial derivatives do not exist there. To deal with this issue, various techniques have been presented. The expansion of finite element method (FEM) has made great progress in recent years [Kwon and Spacone (2002)]. The cohesive zone model (CZM) introduced by Barenblatt [Barenblatt (1959)] brought a significant breakthrough in the computational fracture mechanics. In addition, the concept of the extended finite element method (XFEM) has been introduced to model the crack evolution in the framework of finite element method without remeshing [Belytschko and Black (1999); Moës, Nicolas, Dolbow et al. (2015)]. The cracks could nucleate and propagate through the surface of a finite element, removing the limitations of the CZM that crack can only propagates along the element boundaries. Nevertheless, employing these techniques for complicated discontinuous problem still face the unsastifactory simulation accuracy and efficiency. This motivates a reformulation of classical solid mechanics, which is referred to as Peridynamics [Silling (2000)].

As opposed to traditional approaches, the peridynamic theory reformulates the integral-typed equations, instead of classical partial differential equations. In the peridynamic theory, material points included in a continuous body interact with each other in a neighboring field. The regular bond-based peridynamic models [Silling and Askari (2005)] were widely employed in early times but there are some limitations when using the bond-based peridyamic models [Silling, Epton, Weckner et al. (2007); Silling (2010); Warren, Silling, Askari et al. (2009)]. To avoid the limitations of bond-based peridynamic model, Gerstle et al. [Gerstle, Sau and Silling (2007); Gerstle, Sau and Sakhavand (2009)] proposed the so-called micro-polar peridynamic models by considering the moments of bond. Moreover, a generalized formulation of peridynamic theory was described by Silling et al. [Silling, Epton, Weckner et al. (2007)], which was referred to as state-based peridynamic theory, where individual material particle depends collectively on its interactions with neighboring particles through state variables within the horizon. There are two different types of state-based peridynamic models, ordinary state-based peridynamic model and non-ordinary state-based peridynamic model. The distinction of two state-based peridynamic models is the direction of bond forces. In ordinary state-based peridynamics, bond forces are parallel to the bond. While in non-ordinary state-based peridynamics, there is optional direction of bond forces. Classical constitutive models can be incorporated into the non-ordinary state-based peridynamic model with an approximate nonlocal deformation gradient, which expands the scope of application of the non-ordinary state-based peridynamic model greatly.

The non-ordinary state-based peridynamic theory has been applied successfully to several aspects for fracture and damage problems. For instance, the non-ordinary state-based peridynamic theory was employed by Warren et al. [Warren, Silling, Askari et al. (2009)]

to the solid mechanics problems under dynamic condition. The viscoplasticity model with non-ordinary state-based peridynamic theory was proposed by Foster et al. [Foster, Silling and Chen (2010); Foster, Silling and Chen (2011)]. The stress-based failure criterion was implemented into the non-ordinary state-based peridynamic theory by Zhou et al. [Zhou, Wang and Xu (2016)] to simulate the initiation, propagation and coalescence process of cracks under quasi-static and dynamic loads. Oterkus et al. [Oterkus, Madenci and Agwai (2014)] studied heat conduction problem using state-based peridynamic theory and employed the state-based peridynamics in the formulation for thermoplastic fracture [Amani, Oterkus, Areias et al. (2016)]. Lai et al. [Lai, Liu, Li et al. (2018)] formulated the fracture of quasi-brittle materials under dynamic condition. Fan et al. [Fan, Bergel and Li (2016); Fan and Li (2017)] performed soil fragmentation simulation under blast loads of buried explosive using hybrid PD-SPH method, and Yaghoob et al. [Yaghoobi and Mi (2017)] developed numerical methods in order to improve the stability of peridyamic calculation by suppressing zero-energy mode.

For the damage of concrete materials and structures, Kilic et al. [Kilic and Madenci (2009)] analyzed the influence of interface size and boundary conditions on the critical destabilization load for concrete target. Huang et al. [Huang, Lu and Qiao (2015)] proposed a new method for force loading and a more accurate constitutive model by introducing a quasi-static solution algorithm for local damping and unbalanced force convergence criteria. Gerstle et al. [Gerstle, Sau and Silling (2005); Gerstle, Sau and Silling (2007)] simulated the progressive failure process of concrete and reinforced concrete structures under tension, compression, shear and combined loading conditions.

As to dynamic deformation and simulation of concrete, the effects of strain hardening and strain rate play an important role. Nevertheless, these factors have seldom been taken into account in previous peridynamic simulations. In this paper, the specific purpose is to implement a traditional constitutive model into the non-ordinary state-based peridynamics framework, thus making use of its advantages in simulating impact problems of concrete, considering the effect of strain hardening and strain rate. To accurately characterize the damage progress of concrete, the Holmquist-Johnson-Cook (HJC) model [Holmquist, Johnson and Cook (1993); Johnson, Beissel, Holmquist et al. (1998)] was employed in the present work. The HJC model shows advantages on concrete damage description and large-scale computations, and has been successfully implemented into LS-DYNA, a general-purpose finite element program developed by LSTC (Livermore Software Technology Corporation), for penetration simulations before.

The remainder of this paper is organized as following. In Section 2 the framework of HJC constitutive model is introduced. The brief concept of the peridynamics and the non-ordinary state-based peridynamic theory are presented in Section 3. Section 4 presents the numerical approaches including the discretization of the equation of motion, short range force and the failure criterion. The proposed model and approach are validated in Section 5 with two benchmark numerical examples. Finally, some concluding remarks are drawn in Section 6.

2 The HJC model

In the HJC constitutive model, the normalized equivalent stress is determined by the constitutive relation, as shown in Fig. 1.

$$\sigma^* = \left[A(1-D)+BP^{*N}\right](1+C\ln\dot{\varepsilon}^*) \tag{1}$$

in which σ^* is the normalized equivalent stress, $\sigma^*=\sigma/f_c$. σ and f_c is the actual equivalent stress and the uniaxial compressive strength respectively. P^* is the normalized pressure, and P is the hydrostatic pressure, $P^*=P/f_c$. $\dot{\varepsilon}^*=\dot{\varepsilon}/\dot{\varepsilon}_0$ is the dimensionless strain rate, in which $\dot{\varepsilon}$ is the actual strain rate and $\dot{\varepsilon}_0=10^{-5}\text{s}^{-1}$ is the reference strain rate. In addition, A, B, C and N are material parameters, which are determined by test data. A is the cohesive parameter, B is the pressure hardening coefficient, C is the strain-rate sensitivity coefficient and N is the pressure hardening exponent. Material degradation is described by the damage variable D, leading to reduction of the cohesive strength.

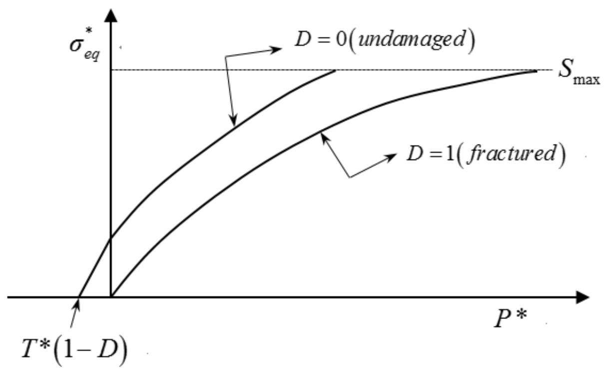

Figure 1: The pressure strength response of the HJC model

Fig. 2 shows the damage response of HJC model, which is defined as the accumulation of equivalent plastic strain increment (caused by plastic shear deformation) and equivalent plastic volumetric strain increment (resulting from plastic crushing of the air voids in the concrete), and is expressed as:

$$D=\sum\frac{\Delta\varepsilon_P+\Delta\mu_P}{\varepsilon_p^f+\mu_p^f}$$
$$\varepsilon_p^f+\mu_p^f=D_1\left(P^*+T^*\right)^{D_2}\geq EFMIN \tag{2}$$

where $\Delta\varepsilon_P$ and $\Delta\mu_P$ are the effective plastic strain increment and plastic volumetric strain during a cycle of integration, respectively. $\varepsilon_p^f+\mu_p^f$ is the plastic strain until concrete fractures under a constant pressure, and $EFMIN$ is a value of the minimum plastic strain causing the fracture of the material, which the value of 0.01 is chosen in our work. D_1 and D_2 represent the damage constants. D_1 is the date from unconfined compression test, while D_2 is chosen to be 1.0, which assumes that plastic fracture strain increases linearly with increasing pressure.

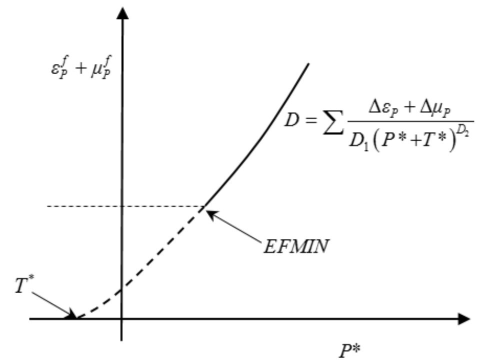

Figure 2: The damage response of the HJC model

The pressure-volume relation of the HJC model is separated into three different phases, as shown in Fig. 3. The first phase (*OA*) is linear elastic from the negative pressure $T(1-D)$ to the crush pressure P_{crush}, where the material undergoes reversible, elastic deformation, and can be expressed as

$$P = K_e\mu, \quad P < P_{crush} \tag{3}$$

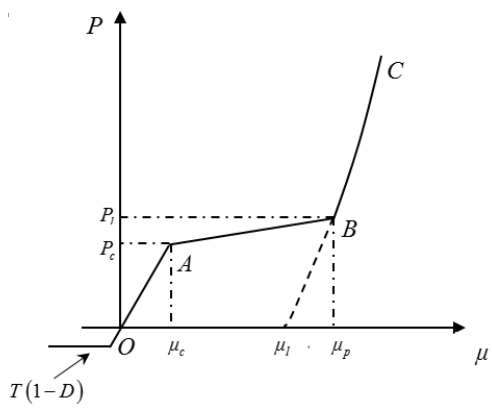

Figure 3: Pressure-volume response of the HJC model

where μ is the volumetric strain, calculated by $\mu = \rho / \rho_0$. ρ and ρ_0 are the current and initial densities respectively. $K = P_{crush} / c_{crush}$ is the elastic bulk modulus.

The second phase (*AB*) is a transitional region, where the air voids in concrete are gradually compressed and the plastic volumetric strain increases. The fracture occurs until the plastic volumetric strain reaches the point (μ_{lock} , P_{lock}).

$$P = P_{lock} + \frac{(P_{lock} - P_{crush})(\mu - \mu_{lock})}{\mu_{lock} - \mu_{crush}}, \quad P_{crush} \le P \le P_{lock} \tag{4}$$

where P_{lock} is the compacting pressure, and μ_{lock} is the locking volumetric strain.

In the third phase (*BC*), all air voids in concrete are crushed out of it. Concrete is locked and cannot be compressed any further in either plastic deformation or void collapse. Therefore, this region can be assumed completely non-linear elastic.

$$P = k_1\bar{\mu} + k_2\bar{\mu}^2 + k_3\bar{\mu}^3, \quad P > P_{lock} \tag{5}$$

where $\bar{\mu} = (\mu - \mu_{lock})/(1+\mu_{lock})$ is the modified volumetric strain, k_1 , k_2 and k_3 are the material constants.

3 Framework of peridynamic theory

3.1 Basic theory

A brief description of peridynamics by Silling [Silling (2000)] is presented below. The peridynamics describes the dynamics process of a body from its reference configuration to the current configuration. A schematic of the body is shown in Fig. 4. In the peridynamics, the motion equation for any material point $\mathbf{x}$ in the reference configuration at time t ($t \geq 0$) is given as

$$\rho\ddot{\mathbf{u}}(\mathbf{x},t) = \mathbf{L}_{\mathbf{u}}(\mathbf{x},t) + \mathbf{b}(\mathbf{x},t) \tag{6}$$

where ρ and $\mathbf{b}$ are the mass density and external applied body force density respectively, $\mathbf{u}(\mathbf{x},t)$ is the displacement field, the initial conditions $\mathbf{u}(\mathbf{x},0) = \mathbf{u}_0(\mathbf{x}), \dot{\mathbf{u}}(\mathbf{x},0) = \dot{\mathbf{u}}_0(\mathbf{x})$. The term $\mathbf{L}_{\mathbf{u}}(\mathbf{x},t)$ is a function of displacement, which represents the internal force density (per unit volume) that is exerted on $\mathbf{x}$ by other body-points [Silling and Lehoucq (2008)]. In the peridynamic theory, the motion of the body is presented by considering the interaction of any material point, $\mathbf{x}$, with the other material points, $\mathbf{x}'$, within a horizon H_x . The size of horizon of a given point $\mathbf{x}$ is finite, defined as $H_x = \{0 < |\mathbf{x} - \mathbf{x}'| < \delta\}$, where $\delta > 0$. The relative position vector between points $\mathbf{x}$ and $\mathbf{x}'$ is referred to as the bond, which is denoted by $\boldsymbol{\xi}$, and is defined as $\boldsymbol{\xi} = \mathbf{x}' - \mathbf{x}$. The bond vector $\boldsymbol{\xi}$ gets deformed under the deformation and the position of point in the deformed configuration is denoted by $\mathbf{y}(\mathbf{x},t) = \mathbf{x} + \mathbf{u}(\mathbf{x},t)$.

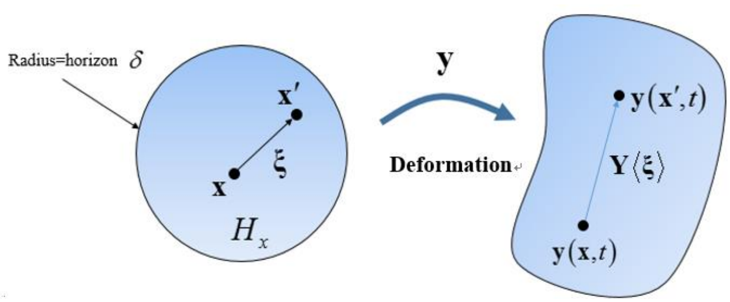

Figure 4: Schematic representation of material particles in the reference and current configuration

In the bond-based peridynamic theory, a pair-wise force function f is used to describe the interaction of material points within a finite distance δ . $\mathbf{L}_{\mathbf{u}}(\mathbf{x},t)$ in Eq. (6) can be expressed as:

$$\begin{aligned}\mathbf{L}_{\mathbf{u}}(\mathbf{x},t) &= \int_{H_x} \mathbf{f}\left(\mathbf{x},\mathbf{x}',\mathbf{u}(\mathbf{x},t),\mathbf{u}(\mathbf{x}',t)\right) dV_{\mathbf{x}'} \\ &= \int_{H_x} \mathbf{f}(\xi,\eta)\, dV_{\mathbf{x}'}\end{aligned} \tag{7}$$

where η is the relative displacement of two interacting material points $\mathbf{x}$ and $\mathbf{x}'$, which is defined as:

$$\eta = \mathbf{u}(\mathbf{x}',t) - \mathbf{u}(\mathbf{x},t) \tag{8}$$

However, in the state-based peridynamic theory, the deformation of the bond is described by the deformation vector state $\underline{\mathbf{Y}}$.

$$\underline{\mathbf{Y}}[\mathbf{x},t]\langle\xi\rangle = \mathbf{y}(\mathbf{x}+\xi,t) - \mathbf{y}(\mathbf{x},t) \tag{9}$$

The equation of motion in state-based peridynamics can be written as:

$$\rho\ddot{\mathbf{u}}(\mathbf{x},t) = \int_{H_x} \left\{\underline{\mathbf{T}}[\mathbf{x},t]\langle\mathbf{x}'-\mathbf{x}\rangle - \underline{\mathbf{T}}[\mathbf{x}',t]\langle\mathbf{x}-\mathbf{x}'\rangle\right\} dV_{\mathbf{x}'} + \mathbf{b}(\mathbf{x},t) \tag{10}$$

Where $\underline{\mathbf{T}}[\mathbf{x},t]$ is the force vector state representing the relationship between material points at time t . To make the notation more concise, (6) will be abbreviated as:

$$\rho\ddot{\mathbf{u}} = \int_{H_x} \left\{\underline{\mathbf{T}}\langle\mathbf{x}'-\mathbf{x}\rangle - \underline{\mathbf{T}}'\langle\mathbf{x}-\mathbf{x}'\rangle\right\} dV_{\mathbf{x}'} + \mathbf{b} \tag{11}$$

where

$$\underline{\mathbf{T}} = \underline{\mathbf{T}}[\mathbf{x},t], \quad \underline{\mathbf{T}}' = \underline{\mathbf{T}}[\mathbf{x}',t] \tag{12}$$

3.2 Constitutive model of non-ordinary state-based peridynamics

To calculate the force-vector state $\mathbf{T}$ mentioned above, the non-local deformation gradient tensor $\mathbf{F}$ of point x is calculated firstly as the following expression

$$\mathbf{F}[\boldsymbol{x},t] = \int_{H_x} \omega(|\boldsymbol{\xi}|)(\underline{\mathbf{Y}} < \boldsymbol{\xi} > \otimes \boldsymbol{\xi}) dV_{\mathrm{x}'} \mathbf{K}^{-1} \tag{13}$$

Where $\omega(|\xi|)$ is the influence function of the bond and $\mathbf{K}$ is the non-local shape tensor defined by

$$\mathbf{K}[\boldsymbol{x},t] = \int_{H_x} \omega(|\boldsymbol{\xi}|)(\boldsymbol{\xi} \otimes \boldsymbol{\xi}) dV_{\mathrm{x}'} \tag{14}$$

It should be noted that the nonlocal shape tensor $\mathbf{K}$ is a symmetric and positive definite second order tensor [Silling, Epton, Weckner et al. (2007)].

The time derivative of $\mathbf{F}$ is defined by

$$\dot{\mathbf{F}} = \int_{H_x} \omega(|\xi|)(\underline{v} \otimes \xi) dV_{\boldsymbol{x}'} \mathbf{K}^{-1} \tag{15}$$

And then, the velocity gradient tensor is given by

$$\mathbf{L} = \dot{\mathbf{F}}\mathbf{F}^{-1} \tag{16}$$

which can be decomposed into symmetric and skew-symmetric parts. The further one is referred to as the rate of deformation tensor $\mathbf{D}$ and is shown as follows:

$$\mathbf{D} = \frac{1}{2}(\mathbf{L} + \mathbf{L}^T) \tag{17}$$

If the polar decomposition theory is applied to $\mathbf{F}$, it can be expressed by

$$\mathbf{F} = \mathbf{VR} = \mathbf{RU} \tag{18}$$

where $\mathbf{R}$ is an orthogonal tensor proposed by Flanagan et al. [Flanagan and Taylor (1987)], representing a rigid-body rotation. And then, $\mathbf{V}$ and $\mathbf{U}$ are the left and right stretch tensors respectively. The velocity gradient tensor can be defined in another way by substituting the right polar decomposition from Eq. (18) into Eq. (16)

$$\mathbf{L} = \dot{\mathbf{R}}\mathbf{R}^{\mathrm{T}} + \mathbf{R}\dot{\mathbf{U}}\mathbf{U}^{-1}\mathbf{R}^{\mathrm{T}} \tag{19}$$

The term $\dot{\mathbf{R}}\mathbf{R}^{\mathrm{T}}$ in Eq. (19) is skew symmetric and describes a rate of rotation. And for completeness, the unrotated rate of deformation tensor $\mathbf{d}$ will be employed.

$$\mathbf{d} = \frac{1}{2}\left[\dot{\mathbf{U}}\mathbf{U}^{-1} + \mathbf{U}^{-1}\dot{\mathbf{U}}\right] = \mathbf{R}_t^{\mathbf{T}}\mathbf{D}\mathbf{R}_t \tag{20}$$

where $\mathbf{R}_t$ describes the rigid-body rotation at current time t, calculated by the incremental formulation as follow:

$$\mathbf{R}_t = \left[\mathbf{I} + \frac{\sin(\Delta t\Omega)}{\Omega}\mathbf{\Omega} - \frac{1-\cos(\Delta t\Omega)}{\Omega^2}\mathbf{\Omega}^2\right]\mathbf{R}_{t-\Delta t} \tag{21}$$

where $\Omega^2 = \omega_i\omega_i$ and $\Omega_{ij} = e_{ikj}\omega_k$. e_{ikj} is the permutation tensor, and the axial vector $\boldsymbol{\omega}$ is given as

$$\boldsymbol{\omega} = \mathbf{w} + \left[\mathbf{I}tr(V) - V\right]^{-1}\mathbf{z} \tag{22}$$

where $\mathrm{w}_i = -\frac{1}{2}e_{ijk}W_{jk}$, $z_i = e_{ikj}D_{jm}V_{mk}$, and $\mathbf{V}_t = \mathbf{V}_{t-\Delta t} + \Delta t\dot{\mathbf{V}}_{\Delta t}$ is the left stretch tensor.

The material is firstly assumed to be elastic, then elastic strain increment tensor and deviatoric strain increment tensor are calculated as

$$\Delta\boldsymbol{e} = \mathbf{d}\Delta t, \quad \Delta\boldsymbol{e}^{dev} = \Delta\boldsymbol{e} - \frac{1}{3}\Delta\boldsymbol{e}\mathbf{I} \tag{23}$$

The trial unrotated Cauchy stress at time t is defined as

$$\boldsymbol{\tau}_t^{\mathrm{trial}} = \boldsymbol{\tau}_{t-\Delta t} + \kappa tr(\Delta\boldsymbol{e})\mathbf{I} + 2\mu\Delta\mathbf{e}^{\mathrm{dev}} \tag{24}$$

where κ and μ are the Lame constants.

According to the von-Mises plasticity theory, we can get the trial deviatoric stress tensor and the von-Mises yield stress as follows:

$$\boldsymbol{S}^{\text{dev}} = \boldsymbol{\tau}_t^{t\text{rial}} - \frac{1}{3} tr\left(\boldsymbol{\tau}_t^{\text{trial}}\right)\mathbf{I} \tag{25}$$

$$S_{VM} = \sqrt{\frac{3}{2}}\left|\boldsymbol{S}^{\text{dev}}\right|, \quad \left|\boldsymbol{S}^{\text{dev}}\right| = \sqrt{S_{ij}^{\text{dev}} S_{ij}^{\text{dev}}} \tag{26}$$

If $S_{VM} < \sigma^* \cdot f_c$, the material is elastic and the unrotated Cauchy stress tensor is equal to the trial unrotated Cauchy stress tensor. Otherwise, the stress state of the material is beyond the yield surface, indicating that the von-Mises yield stress needs to be updated from the HJC model. For the HJC model, the equivalent plastic strain increment tensor can be required by Eq. (27):

$$\Delta e_{t-\Delta t/2} - \Delta\lambda_{t-\Delta t/2} - \frac{1}{2\mu}\left[\sqrt{\frac{2}{3}} f\left(\sigma, \dot{\varepsilon}\right) - S_{t-\Delta t}\right] = 0 \tag{27}$$

Then, the rotated Cauchy stress tensor $\boldsymbol{\sigma}$ is based on the unrotated Cauchy stress as follow

$$\boldsymbol{\sigma} = \mathbf{R}\boldsymbol{\tau}\mathbf{R}^T \tag{28}$$

And the first Piola-Kirchhoff stress tensor $\mathbf{P}$ is calculated as

$$\mathbf{P} = \left(J\boldsymbol{\sigma}\right)\mathbf{F}^{-T}$$

Then, the force vector state of the bond $\boldsymbol{\xi}$ can be expressed as

$$\mathbf{T}\langle\xi\rangle = \omega\langle\xi\rangle \mathbf{PK}^{-1}\xi \tag{29}$$

4 Numerical implementation

4.1 Discretization

To solve the integral equation of peridynamics, the governing equations of motion Eq. (10) can be numerically discretized as follows:

$$\rho\ddot{\mathbf{u}}_{\text{i}}^n = \sum_p \left\{\underline{\mathbf{T}}\left[\mathbf{x}_i^n, t^n\right]\left\langle\mathbf{x}_p^n - \mathbf{x}_i^n\right\rangle - \underline{\mathbf{T}}\left[\mathbf{x}_p^n, t^n\right]\left\langle\mathbf{x}_i^n - \mathbf{x}_p^n\right\rangle\right\} V_p + \mathbf{b}\left(\mathbf{x}_i^n, t^n\right) \tag{30}$$

where n is the number of time steps, $V_p = |\Delta\mathbf{x}|^3$ stands for the involved volume of particle $\mathbf{x}_p$, $\ddot{\mathbf{u}}_{\text{i}}^n$ and $\ddot{\mathbf{u}}^{n+1}$ are the acceleration of point $\mathbf{x}_i$ at time t^n and t^{n+1} respectively.

The displacement of point $\mathbf{x}_i$ at time t^{n+1} can be obtained from the equation in Eqs. (31)-(32), which is based on an explicit Verlet-Velocity difference formula [Parks, Seleson, Plimpton et al. (2011)].

$$\dot{u}_i^{n+1} = \dot{u}_i^n + \frac{\Delta t}{2\rho}\left(\mathbf{L}_{\mathbf{u}} + \mathbf{b}\right) + \frac{\Delta t}{2\rho}\left(\mathbf{L}_{\mathbf{u}} + \mathbf{b}\right)^{n+1} \tag{31}$$

$$u_i^{n+1} = u_i^n + \dot{u}_i^n \Delta t + \frac{(\Delta t)^2}{2\rho}\left(\mathbf{L_u} + \mathbf{b}\right)^n \tag{32}$$

where Δt is the time step, and in order to obtain a stable numerical result, the time step Δt should be satisfied the following inequation [Warren, Silling, Askari et al. (2009)].

$$\Delta t \propto \frac{\delta}{c'} \tag{33}$$

where δ denotes the size of horizon, $c' = \sqrt{(\lambda + 2\mu)/\rho}$ represents the dilatational wave speed, λ and μ are the Lame's elastic constants of the material.

4.2 Short range force

When simulating the movement of the material point in the target substance, a short-range force model [Silling and Askari (2005)] is employed to prevent target material points from penetrating each other, as shown in Fig. 5.

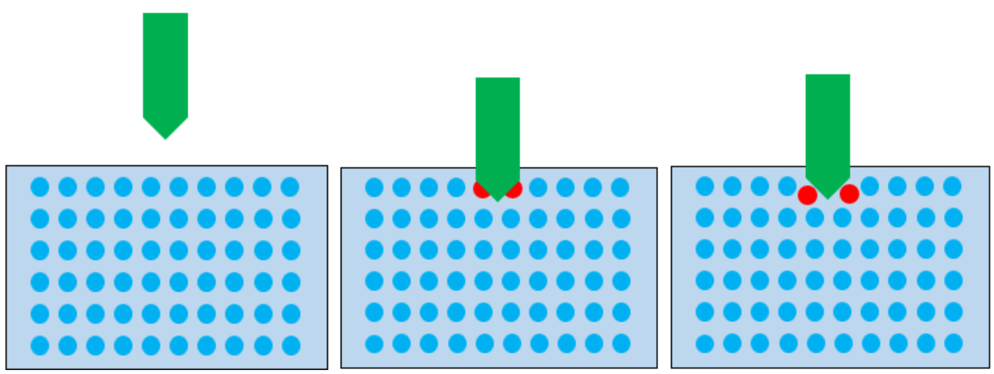

Figure 5: Contact model with short range force

The short-range force between material points can be expressed by

$$\boldsymbol{f}_s\left(\boldsymbol{y}_p, \boldsymbol{y}_i\right) = \min\{0, \frac{c_{sh}}{\delta}(\left\|\boldsymbol{y}_p - \boldsymbol{y}_i\right\| - d_{pi})\}\frac{\boldsymbol{y}_p - \boldsymbol{y}_i}{\left\|\boldsymbol{y}_p - \boldsymbol{y}_i\right\|} \tag{34}$$

where $\boldsymbol{y}$ is the position of different material point. $c_{sh} = 1.5c$, c is the micro-modulus of the material, $c = (12\mathrm{E})/(\pi\delta^4)$. d_{pi} is the distance between material point p and i, and it can be defined by

$$d = \min\left\{0.9\left\|\boldsymbol{x}' - \boldsymbol{x}\right\|,\ 1.35\left|\Delta \boldsymbol{x}\right|\right\} \tag{35}$$

4.3 Failure criterion

In this paper, damage is given as the ratio shown in Eq. (36), which is relevant to the amount of broken bonds and the total amount of bonds in the horizon as:

$$D(x,t)=1-\frac{\int_{H_x}\mu(x,\xi,t)\,dV_{x'}}{\int_{H_x}dV_{x'}} \tag{36}$$

where $\mu(x,\xi,t)$ is a breakage factor of the bond

$$\mu(x,\xi,t)=\begin{cases}1 & s(t',\xi)<s_0,\ 0<t'<t\\ 0 & else\end{cases} \tag{37}$$

where s denotes the stretch of a bond, $s=\frac{|\eta+\xi|-|\xi|}{|\xi|}$, and s_0 stands for the critical stretch or failure of the bond, $s_0=\sqrt{\frac{5G_0}{9k\delta}}$, where G_0 is energy release rate [Silling and Askari (2005)].

5 Numerical results

In this section, two benchmark examples are considered to validate and demonstrate the proposed peridynamic model. In the first example, the fracture of a single-edge notched, three-point-bending concrete beam under impact loading is analyzed. The experimental results were reported by John et al. [John and Shah (1986)] and John [John (1988)]. In the second example, the penetration experiment conducted by Hanchak et al. [Hanchak, Forrestal, Young et al. (1992)] is conducted. The results of the proposed peridynamic model are compared with available experimental results.

The material parameters for concrete by using the HJC model are listed in Tab. 1. For the second benchmark example, the material parameters for steel bars in the concrete and steel projectiles are: Young's modulus $E=206\,\text{Gpa}$, density $\rho=7856.3\,\text{kg/m}^3$, Poisson's ratio $v=0.28$, and Yield Stress $\sigma_y=345\,\text{Mpa}$ (the projectile is considered as a rigid body with an ultrahigh elastic modulus, and Yield Stress $\sigma_y=1720\,\text{Mpa}$) [Hanchak, Forrestal, Young et al. (1992)].

Table 1: Material parameters for concrete using HJC constitutive model

$\rho_0\left(\text{kg/m}^3\right)$	$G(\text{Mpa})$	υ	A	B	N	C
2440	14.86	0.2	0.79	1.6	0.61	0.007
$S_{\max}$	$f_c(\text{Mpa})$	$f_t(\text{Mpa})$	$\dot{\varepsilon}\left(\text{s}^{-1}\right)$	D_1	D_2	$\left(\varepsilon_{\text{p}}^{\text{f}}\right)_{\min}$
7	48	4	1x10^{-5}	0.04	1	0.01
$P_{\text{crush}}(\text{Mpa})$	μ_{crush}	$P_{\text{lock}}(\text{Mpa})$	μ_{lock}	$K_1(\text{Mpa})$	$K_2(\text{Mpa})$	$K_3(\text{Mpa})$
16	0.001	800	0.1	85	-171	208

5.1 Crack propagation in a three-point-bending specimen under dynamic condition

In the three-point-bending impact test, the concrete specimen with an initial notch is subjected to impact loading (see Fig. 6). The experiment reported the crack propagation paths for several test specimens with the offset notch at different locations, and Belytschko et al. predicted the crack propagation angles and time data by element-free Galerkin (EFG) method [Belytschko, Organ and Gerlach (2000)]. The location of the notch in the concrete specimen is described by a normalized parameter γ, which is the ratio of the distance from the notch to the midspan to the distance from one support to the midspan. And the height of the notch is decided by a parameter β, which is the ratio between notch height and specimen height.

The following parameters are same as the experiments: the distance from the midspan to the support is 101 mm, the distance from the support to the edge is 13 mm, the height of the specimen is 76 mm, and the thickness of the specimen is 25.4 mm. To effectively decrease the inertial oscillations, the impact velocity is increased linearly to the maximum value v_1 and then held unchanged

$$v(t) = \begin{cases} v_1 t / t_1 & t \le t_1 \\ v_1 & t > t_1 \end{cases}$$

where $t_1 = 1.96 \times 10^{-4}$ s; $v_1 = 0.065$ m/s.

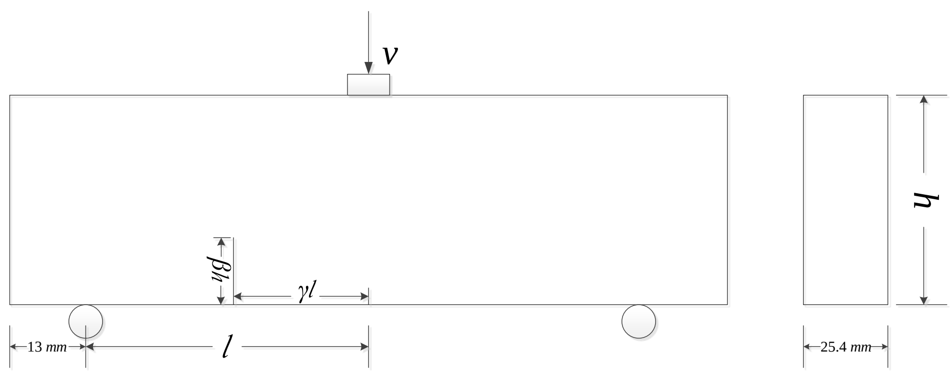

Figure 6: Concrete specimen with offset notch under dynamic condition

In the numerical model, the specimen is discretized to 139188 material points with a spacing of 1 mm. The time step is adopted as 6.0×10^{-7} s and the horizon size is δ=3 mm.

Fig. 7 shows the crack propagation path of the three-point-bending specimen with γ = 0.5. We can see that the crack firstly initiates from the notch tip, then curves gradually toward the vertical midline of the three-point-bending specimen (the loading point). Eventually, it intersects with the upper edge. The initial direction of the fracture is 21.84° and the fracture starts propagating at 640 μs.

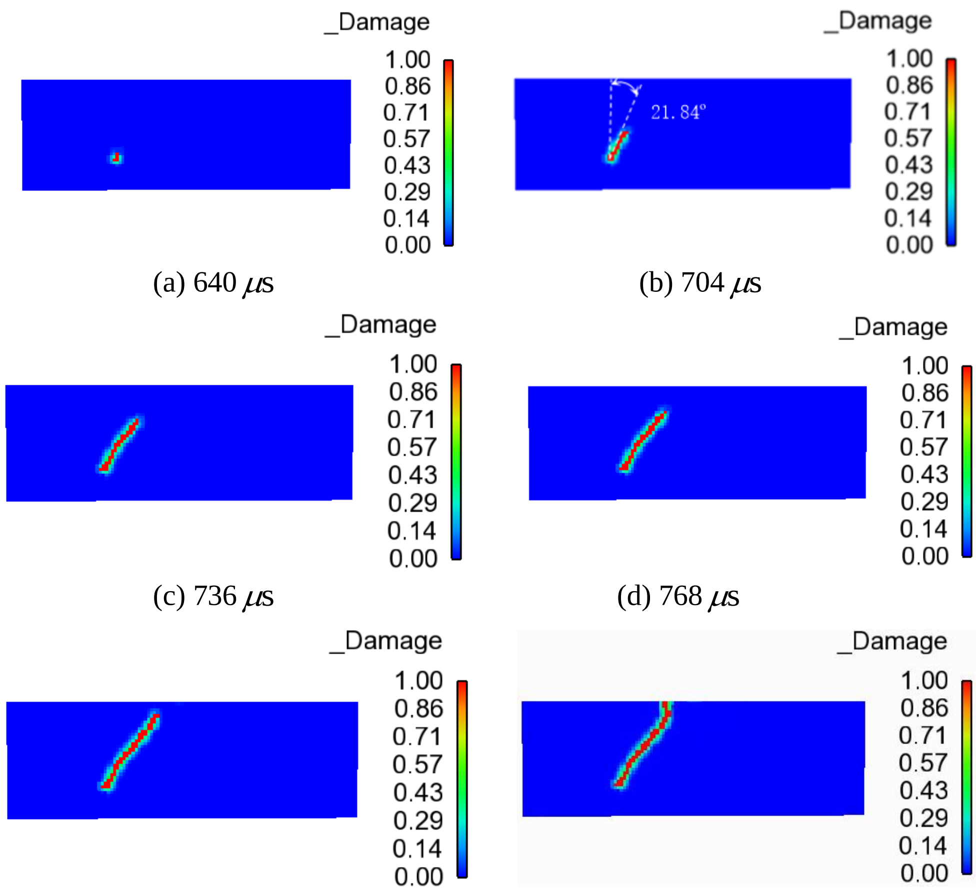

(a) 640 μs (b) 704 μs

(c) 736 μs (d) 768 μs

(e) 864 μs (f) 960 μs

Figure 7: Damage maps of the crack in the three-point-bending specimen

Fig. 8 shows the crack paths of the specimen with γ = 0.0 and 0.72 respectively. To verify the proposed peridynamic model, experimental observations and results by using LEFM method are presented for comparison (see Fig. 9). It shows that the crack propagation paths and initial propagation directions (the angle θ)predicted by the proposed model are in compared well with the experimental results and LEFM prediction.

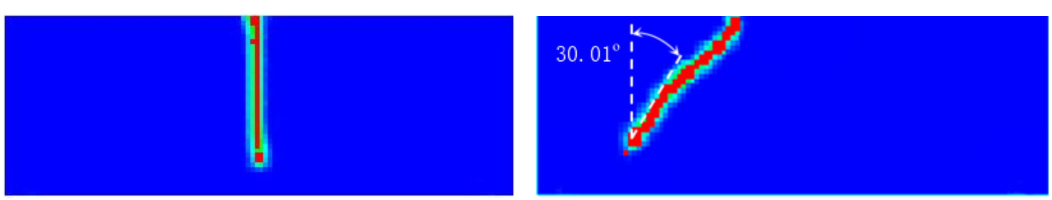

(a) γ =0.0 (b) γ =0.72

Figure 8: Crack propagation paths of the three-point-bending specimen

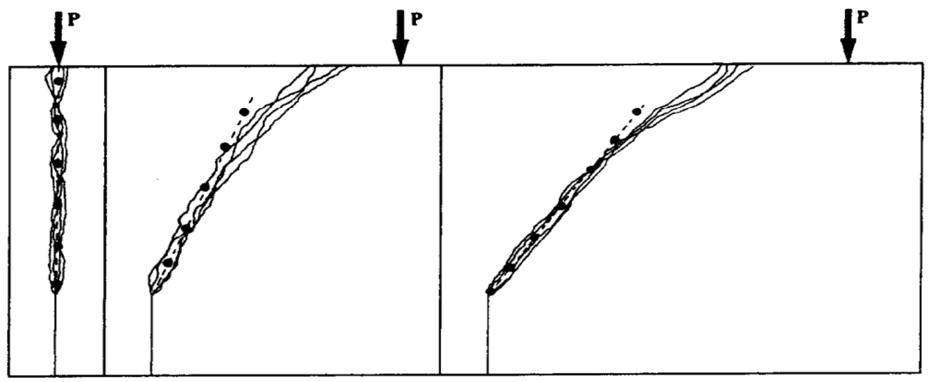

Figure 9: Crack propagation paths of the three-point-bending specimen (experimental and LEFM results [Belytschko, Organ and Gerlach (2000)])

To determine the relationship between crack propagation path and different location of notch, the results of cracking angle and crack initiation time with different γ are listed in Tab. 2. It shows that no matter where the pre-existed notch located, all the cracks propagate from the notch tip towards the loading point. As the γ increases, the initial angle and crack initiation time will increase.

Table 2: Crack propagation angles and time data from peridynamic simulation

γ	The initial directions/°	The initiation time/μs
0	0	480
0.34	17.21	544
0.5	21.84	640
0.67	26.81	736
0.72	29.84	896

5.2 Hanchak penetration experiment

In the Hanchak penetration experiment, a rectangular block of reinforced concrete suffers from projectile impact. Fig. 10 and Fig. 11 show the geometry of the target and location of the reinforcement. The impact point is not the center of the specimen so as to avoid the collision between the projectile and steel bars. For the sake of numerical calculation, the models are discretized into particles with the uniform grid spacing $\Delta x = 5\ \mathrm{mm}$. In the numerical model, the specimen is discretized to 570972 material points. The stable time step is adopted of 8.0×10^{-7} s and the horizon size is three times of grid spacing, δ=15 mm.

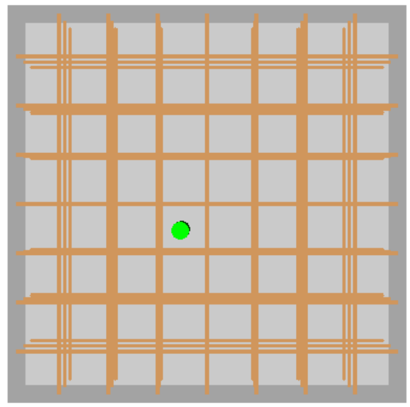

Figure 10: Steel projectile and reinforced concrete target

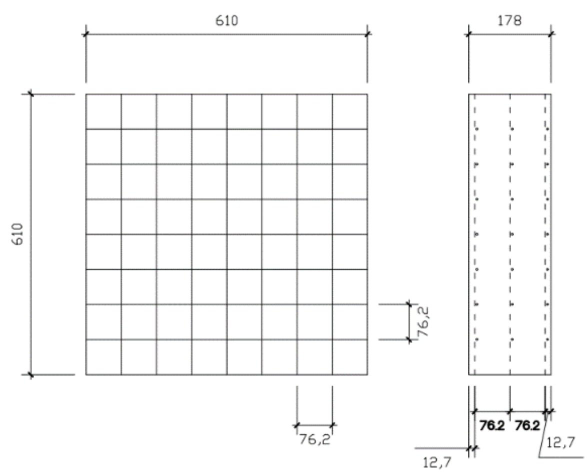

Figure 11: Geometry of the steel reinforced block (mm)

Fig. 12 shows the post-test photographs of impact and exit surfaces for concrete under a nominal striking velocity of 750 m/s in experiment, reflecting the craters caused by spallation. The whole impact failure process of the concrete at striking velocity of 750 m/s during perforation by using the proposed peridynamic method is plotted in Fig. 13 and Fig. 14, with damage maps of the impact surface and damage maps of the exit surface respectively. It shows that the numerical results on the pattern of damage distribution agree well with the experimental observations.

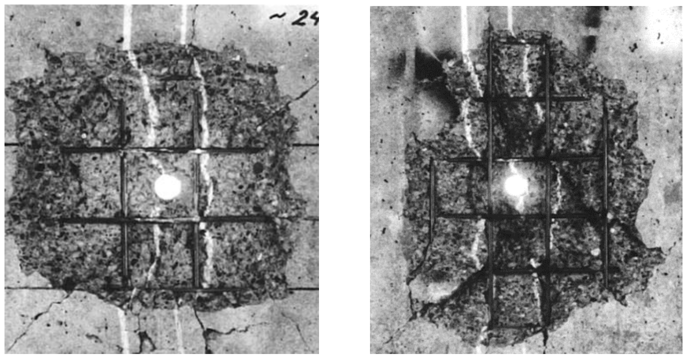

(a) impact surface (b) exit surface

Figure 12: Post-test surface of the reinforced concrete block at a nominal striking velocity of 749 m/s [Hanchak, Forrestal, Young et al. (1992)]

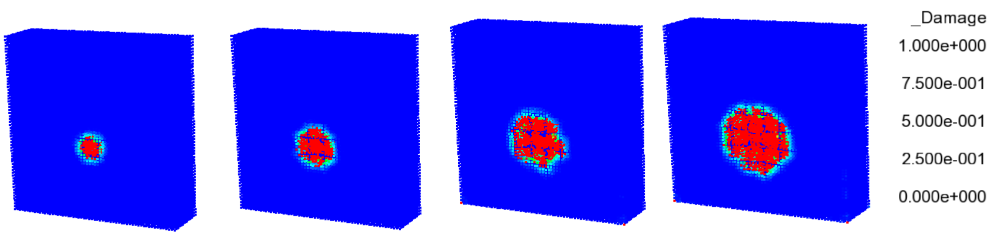

(a) 110 μs (b) 210 μs (c) 340 μs (d) 450 μs

Figure 13: Damage maps on the impacting surface

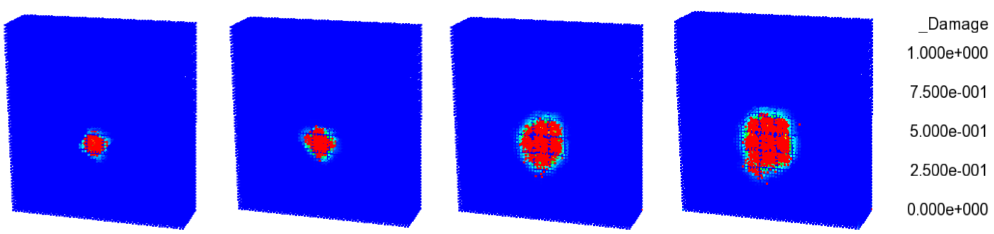

(a)170 μs (b) 220 μs (c) 380 μs (d) 440 μs

Figure 14: Damage maps on the exit surface

Fig. 15 shows the contours of the von-Mises stress observed from the exit surface of the specimen. In the early time, when the stress wave arrives the exit surface, it propagates to the edge uniformly, as shown in Figs. 15(a) and (b). As damage accumulates, the non-uniform propagation of the stress wave can be found in the target (Figs. 15 (c) and 15(d)).

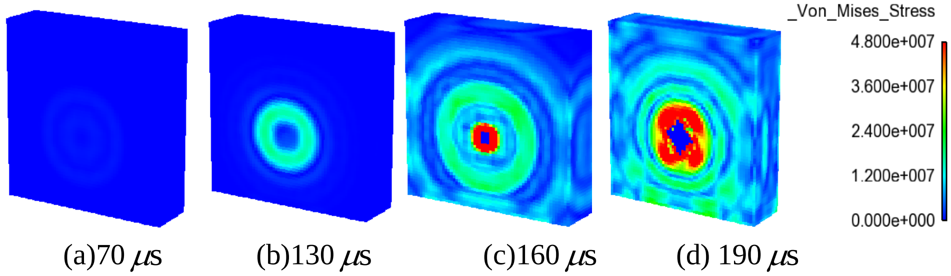

Figure 15: Contour of the von-Mises stress on the exit surface

Compared to the results with different impacting velocities between 300 m/s and 1100 m/s in experiment, the failure of the target with six impacting velocities 301 m/s, 381 m/s, 434 m/s, 606 m/s, 749 m/s, and 1058 m/s were analyzed by using the proposed peridynamic model, and the residual velocities are predicted. The residual velocities by using the proposed peridynamic approach and experiment results are listed in Fig. 16. It shows that the numerical results match well with experimental data, indicating that the proposed peridynamic approach is capable of analyzing this kind of impacting problems.

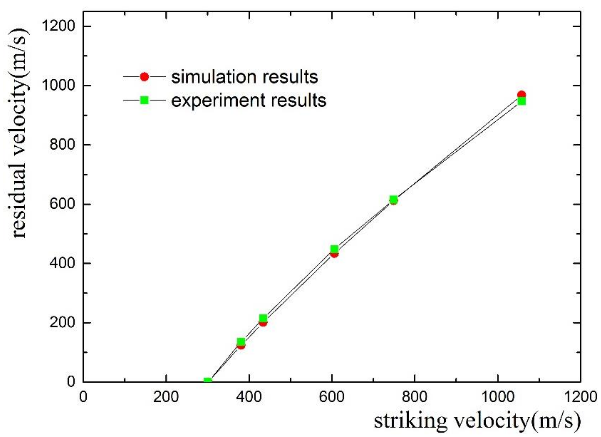

Figure 16: Comparison of residual velocities of the projectile with various striking velocities between the numerical results and experimental results [Hanchak, Forrestal, Young et al. (1992)]

6 Conclusions

In this work, a non-ordinary state-based peridynamic model for concrete failure process simulation under impact loading is presented by reformulating the HJC constitutive model for concrete in continuum mechanics theory. In the proposed model, the strain hardening, strain-rate effects, and pressure-dependence is taken into account, to characterize the damage and dynamic fracture of concrete under impacting loads.

Two benchmark problems have been studied to verify the proposed model and approach. In the dynamic fracture of a three-point-bending beam, the crack propagation paths of the specimen subjected to impact loading were investigated, and crack propagation, orientation and cracking time with offset notches at different locations were analyzed. The results show that when the pre-existing notch is closer to edge of the specimen, the cracking angle and initiation time will increase. This agrees well with available experimental observations and results from other numerical methods. In the Hanchak penetration test, the evolution of damage and stress wave in the target at a nominal striking velocity of 749 m/s was investigated. The residual velocities of the projectile with different impacting velocities were predicted by using the proposed model, and which keeps good accordance with experimental results. This indicates the capability of the proposed non-ordinary state-based peridynamic model to simulate the deformation, damage and fracture of concrete structures subjected to dynamic loads such as impacting.

Acknowledgement: The authors acknowledge the support from the National Key R&D Program of China (No. 2018YFC0406703), National Natural Science Foundation of China (No. 51679077) and the Fundamental Research Funds for the Central Universities in China (No. 2015B18314, 2017B13014).

References

Amani, J.; Oterkus, E.; Areias, P.; Zi, G.; Nguyen-Thoi, T. et al. (2016): A non-ordinary state-based peridynamics formulation for thermoplastic fracture. *International Journal of Impact Engineering, SI: Experimental Testing and Computational Modeling of Dynamic Fracture*, vol. 87, pp. 83-94.

Barenblatt, G. I. (1959): The formation of equilibrium cracks during brittle fracture. General ideas and hypotheses. Axially-symmetric cracks. *Journal of Applied Mathematics and Mechanics*, vol. 23, no. 3, pp. 622-636.

Belytschko, T.; Black, T. (1999): Elastic crack growth in finite elements with minimal remeshing. *International Journal for Numerical Methods in Engineering*, vol. 45, no. 5, pp. 601-620.

Belytschko, T.; Organ. D.; Gerlach, C. (2000): Element-free galerkin methods for dynamic fracture in concrete. *Computer Methods in Applied Mechanics & Engineering*, vol. 187, no. 3, pp. 385-399.

Ben-Dor, G.; Dubinsky, A.; Elperin, T. (2005): Ballistic impact: recent advances in analytical modeling of plate penetration dynamics: A review. *Applied Mechanics Reviews*, vol. 58, no. 1, pp. 355-371.

Bićanić, N.; Zienkiewicz, O. C. (2010): Constitutive model for concrete under dynamic loading. *Earthquake Engineering & Structural Dynamics*, vol. 11, no. 5, pp. 689-710.

Børvik, T.; Langseth, M.; Hopperstad, O. S. (2002): Ballistic perforation resistance of high performance concrete slabs with different unconfined compressive strengths. *High Performance Structures & Composites*, pp. 273-282.

Corbett, G. G.; Reid, S. R.; Johnson, W. (1996): Impact loading of plates and shells by free-flying projectiles: A review. *International Journal of Impact Engineering*, vol. 18, no. 2, pp. 141-230.

Fan, H.; Bergel, G. L.; Li, S. (2016): A hybrid peridynamics-SPH simulation of soil fragmentation by blast loads of buried explosive. *International Journal of Impact Engineering*, vol. 87, pp. 14-27.

Fan, H.; Li, S. (2017): A peridynamics-SPH modeling and simulation of blast fragmentation of soil under buried explosive loads. *Computer Methods in Applied Mechanics & Engineering*, vol. 318, pp. 349-381.

Flanagan, D. P.; Taylor, L. M. (1987): An accurate numerical algorithm for stress integration with finite rotations. *Computer Methods in Applied Mechanics & Engineering*, vol. 62, no. 3, pp. 305-320.

Foster, J. T.; Silling, S. A.; Chen, W. W. (2010): Viscoplasticity using peridynamics. *International Journal for Numerical Methods in Engineering*, vol. 81, no. 10, pp. 1242-1258.

Foster, J. T.; Silling, S. A.; Chen, W. W. (2011): An energy-based failure criterion for use with peridynamic states. *International Journal for Multiscale Computational Engineering*, vol. 9, no. 6, pp. 675-687.

Gerstle, W.; Sau, N.; Silling, S. A. (2005): Peridynamic modeling of plain and reinforced concrete structures. *18th International Conference on Structural Mechanics in Reactor Technology*, pp. 54-68.

Gerstle, W.; Sau, N.; Silling, S. (2007): Peridynamic modeling of concrete structures. *Nuclear Engineering & Design*, vol. 237, no. 12, pp. 1250-1258.

Gerstle, W.; Sau, N.; Aguilera, E. (2007): Micropolar peridynamic modeling of concrete structures. *Proceedings of the 6th International Conference on Fracture Mechanics of Concrete Structures*, pp. 1-8.

Gerstle, W. H.; Sau, N.; Sakhavand, N. (2009): On peridynamic computational simulation of concrete structures. *American Concrete Institute Special Publication*, pp. 245-265.

Hanchak, S. J.; Forrestal, M. J.; Young, E. R.; Ehrgott, J. Q. (1992): Perforation of concrete slabs with 48 MPa (7 ksi) and 140 MPa (20 ksi) unconfined compressive strengths. *International Journal of Impact Engineering*, vol. 12, no. 12, pp. 1-7.

Holmquist, T. J.; Johnson, G. R.; Cook, W. H. (1993): A computational constitutive model for concrete subjected to large strains, high strain rates and high pressures. *Proceedings of 14th International Symposium on Ballistics*, pp. 591-600.

Huang, D.; Lu, G.; Qiao, P. (2015): An improved peridynamic approach for quasi-static elastic deformation and brittle fracture analysis. *International Journal of Mechanical Sciences*, vol. 94-95, pp. 111-122.

Johnson, G. R.; Beissel, S. R.; Holmquist, T. J.; Frew, D. J. (1998): Computer radial stresses in a concrete target penetrated by a steel projectile. *Proceedings of structures under shock and impact V*, pp. 793-806.

John, R.; Shah, S. P. (1986): Fracture of concrete subjected to impact loading. *Journal of Structural Engineering*, vol. 116, no. 3, pp. 585-602.

John, R. (1988): *Mixed Mode Fracture of Concrete Subjected to Impact Loading* (*Ph.D. Thesis*). Northwestern University, United States.

Kennedy, R. P. (1976): A review of procedures for the analysis and design of concrete structures to resist missile impact effects. *Nuclear Engineering and Design*, vol. 37, no. 2, pp. 183-203.

Kilic, B.; Madenci, E. (2009): Structural stability and failure analysis using peridynamic theory. *International Journal of Non-Linear Mechanics*, vol. 44, no. 8, pp. 845-854.

Kwon, M.; Spacone, E. (2002): Three-dimensional finite element analyses of reinforced concrete columns. *Computers & Structures*, vol. 80, no. 2, pp. 199-212.

Lai, X.; Liu, L. Sh.; Li, S. F.; Zeleke, M.; Liu, Q. et al. (2018): A non-ordinary state-based peridynamics modeling of fractures in quasi-brittle materials. *International Journal of Impact Engineering*, vol. 111, pp. 130-146.

Leppänen, J. (2006): Concrete subjected to projectile and fragment impacts: Modelling of crack softening and strain rate dependency in tension. *International Journal of Impact Engineering*, vol. 32, no. 11, pp. 1828-1841.

Li, Q. M.; Reid, S. R.; Wen, H. M.; Telford, A. R. (2005): Local impact effects of hard missiles on concrete targets. *International Journal of Impact Engineering*, vol. 32, no. 1, pp. 224-284.

Liu, H. F.; Ning, J. G. (2008): Dynamic constitutive model of concrete subjected to impact loading. *Engineering Mechanics*, vol. 10, no. 8, pp. 135-140.

Moës, N.; Dolbow, J.; Belytschko, T. (2015): A finite element method for crack growth without remeshing. *International Journal for Numerical Methods in Engineering*, vol. 46, no. 1, pp. 131-150.

Oterkus, S.; Madenci, E.; Agwai, A. (2014): Peridynamic thermal diffusion. *Journal of Computational Physics*, vol. 265, no. 10, pp. 71-96.

Parks, M. L.; Seleson, P.; Plimpton, S. J. (2011): Peridynamics with Lammps: a user guide v0.3 beta. *Sandia Report SAND2011-8523*, Sandia National Laboratories, New Mexico.

Silling, S. A. (2000): Reformulation of elasticity theory for discontinuities and long-range forces. *Journal of Mechanics Physics of Solids*, vol. 48, no. 1, pp. 175-209.

Silling, S. A.; Askari, E. (2005): A meshfree method based on the peridynamic model of solid mechanics. *Computers & Structures*, vol. 83, no. 17, pp. 1526-1535.

Silling, S. A.; Epton, M.; Weckner, O.; Xu, J.; Askari, A. (2007): Peridynamics states and constitutive modeling. *Journal of Elasticity*, vol. 88, no. 2, pp. 151-184.

Silling, S. A; Lehoucq, R. B. (2008): Convergence of peridynamics to classical elasticity theory. *Journal of Elasticity*, vol. 93, no. 1, pp. 13-37.

Silling, S. A. (2010): Linearized theory of peridynamic states. *Journal of Elasticity*, vol. 99, no. 1, pp. 85-111.

Silling, S. A. (2017): Stability of peridynamic correspondence material models and their particle discretizations. *Computer Methods in Applied Mechanics & Engineering*, vol. 322, pp. 42-57.

Tai, Y. S.; Tang, C. C. (2006): Numerical simulation: the dynamic behavior of reinforced concrete plates under normal impact. *Theoretical & Applied Fracture Mechanics*, vol. 45, no. 2, pp. 117-127.

Teng, T. L.; Chu, Y. A.; Chang, F. A.; Chin, H. S. (2005): Numerical analysis of oblique impact on reinforced concrete. *Cement & Concrete Composites*, vol. 27, no. 4, pp. 481-492.

Tuniki, B. K. (2012): *Peridynamic Constitutive Model for Concrete* (*Ph.D. Thesis*). University of New Mexico, United States.

Warren, T. L.; Silling, S. A.; Askari, A.; Weckner, O.; Epton, M. A. et al. (2009): A non-ordinary state-based peridynamic method to model solid material deformation and fracture. *International Journal of Solids & Structures*, vol. 46, no. 5, pp. 1186-1195.

Yaghoobi, A.; Mi, G. C. (2015): Meshless modeling framework for fiber reinforced concrete structures. *Computers and Structures*, vol. 161, pp. 43-54.

Yaghoobi, A.; Mi, G. C. (2017): Higher-order approximation to suppress the zero-energy mode in non-ordinary state-based peridynamics. *Computers & Structures*, vol. 188, pp. 63-79.

Zhou, X.; Wang, Y.; Xu, X. (2016): Numerical simulation of initiation, propagation and coalescence of cracks using the non-ordinary state-based peridynamics. *International Journal of Fracture*, vol. 201, pp. 213-34.